2012

Carbon Dioxide Separation with a Two-Dimensional Polymer Membrane

Joshua Schrier
*Haverford College,* jschrier@haverford.edu

Carbon Dioxide Separation with a Two-Dimensional Polymer Membrane

Joshua Schrier*

Department of Chemistry, Haverford College, Haverford, Pennsylvania 19041, United States

S *Supporting Information*

ABSTRACT: Carbon dioxide gas separation is important for many environmental and energy applications. Molecular dynamics simulations are used to characterize a two-dimensional hydrocarbon polymer, PG-ES1, that uses a combination of surface adsorption and narrow pores to separate carbon dioxide from nitrogen, oxygen, and methane gases. The CO_2 permeance is 3×10^5 gas permeation units (GPU). The CO_2/N_2 selectivity is 60, and the CO_2/CH_4 selectivity exceeds 500. The combination of high CO_2 permeance and selectivity surpasses all known materials, enabling low-cost postcombustion CO_2 capture, utilization of landfill gas, and horticulture applications.
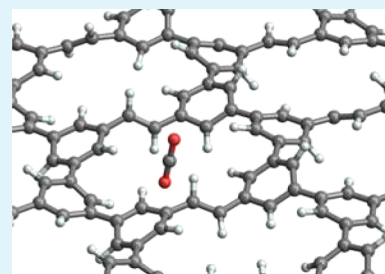
KEYWORDS: *porous graphene, two-dimensional polyphenylene, E-stilbene, Langmuir adsorption, membrane separation, carbon capture, molecular dynamics*

INTRODUCTION

The emerging consensus that anthropogenic greenhouse gas emissions have an impact on climate[1] has motivated the study of carbon dioxide capture. Separating carbon dioxide from nitrogen, oxygen, and methane is challenging because of the similar sizes and intermolecular interactions, and existing methods all have practical disadvantages.[2] Adsorption methods require a large quantity of liquid or solid sorbent that must be regenerated with a pressure or temperature change to desorb the gas molecules.[2] Membrane-based gas separation can be more efficient and economical because it avoids the energy cost of liquefying the gases needed for cryogenic distillation, and the large size and high maintenance associated with pressure- and temperature- swing adsorption processes on solid sorbents or in liquid amine solutions.[3] However, existing polymeric,[4,5] amorphous carbon,[2,6] and metal−organic framework[2,7] (MOF) membranes do not have high enough permeance or selectivity for economically viable CO_2 separations.[8−10]

Although graphene is impermeable to gases,[11,12] introducing small pores allows for highly selective membrane separation of aqueous ions,[13] liquid water,[14] and gases.[15] Recent work has identified experimentally synthesized two-dimensional nanoporous graphene-like materials capable of industrially relevant gas separations. For example, "porous graphene"——also called two-dimensional polyphenylene (2D-PP)—— synthesized by Bieri et al.[16] has been proposed for efficient separation of H_2 from CH_4, CO_2, and CO,[17,18] and the separation of He from CH_4.[18,19] Another example, graphdiyne synthesized by Li et al.,[20] has been proposed for separating H_2 from CH_4 and CO.[21] All of these separations rely on size-exclusion by the subnanometer pores. (The small size of the pores also lead to quantum mechanical effects that allow for isotope separation,[19,22−25] but this is outside the purely classical scope of this paper.)

An intriguing exception was seen in recent simulations by Du et al., in which (larger) N_2 molecules were more likely to be transmitted than (smaller) H_2 molecules through single holes in an otherwise impermeable graphene sheet.[26] The stronger dispersion interaction of N_2 causes preferential adsorption to the graphene surface, whereas the weaker dispersion interaction of H_2 causes it to remain predominantly in the gas phase. Besides increasing the concentration of molecules near the pore, the adsorbed molecules moving along the surface can potentially find the pore more readily than a molecule in the gas phase. A basic proof in statistical physics is that a two-dimensional random walk always finds an absorbing target object, but the probability is less than one in three-dimensions.[27] (One variant, the "narrow escape problem" of a diffusing particle searching for a circular exit hole in a spherical cavity upon whose surface the gas can adsorb and desorb, was very recently solved analytically by Berezhovskii and Barzykin.[28]) Thus, the N_2 molecules adsorbed on the surface are more likely to find the pores than the H_2 molecules in the gas phase. This surface adsorption effect was not seen in previous studies of nanoporous graphene gas separation[17−19,21] that considered Arrhenius and transition state theory estimates of the rate using gas phase reactants and products rather than surface adsorbed molecules, nor in previous ab initio molecular dynamics simulations[15] that were performed at too high a temperature (600 K) to observe surface adsorption. Recent work has considered adsorption of molecules on the surface of nanoporous graphenes,[29,30] only in the context of pressure- and temperature-swing adsorption separation of CO_2 but not for membrane separations.
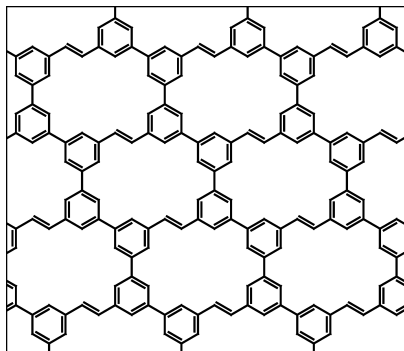
Because the larger polarizability and quadrupole moment of CO_2 relative to N_2, O_2, and CH_4 enhances its adsorption on 2D-PP and graphene,[29] I investigated the use of this strategy for CO_2 separation in conjunction with a properly designed nanoporous structure. The material in Chart 1 accomplishes

Chart 1. PG-ES1

this goal. It is denoted PG-ES1 (Porous Graphene-E-Stilbene-1), because it is analogous to the "porous graphene" (2D-PP) structure synthesized by Bieri et al.,[16] but extended in one direction by an E-stilbene-like unit. Conceptually, the effective pore size (defined by the van der Waals radii of the hydrogen atoms) in PG-ES1 is greater than in 2D-PP, but still smaller than van der Waals diameters of the gas molecules to be separated. The repulsive intermolecular interactions create a potential energy barrier for passage of the gas molecules that is too high for methane and only feasible for the linear molecules oriented along their narrow axis, but with a smaller magnitude than in 2D-PP. The repulsive interactions for CO_2 are smaller than those for O_2 and N_2, because its electron density distribution is slightly narrower, increasing the relative probability of CO_2 passage.

Exploratory calculations on larger E-stilbene and phenyl-extended pores gave higher permeance, but very low CO_2/N_2 and CO_2/CH_4 selectivities. These larger structures have effective pore sizes that are greater than the van der Waals diameters of the molecules, resulting in attractive (or only slightly repulsive) intermolecular interaction rather than the repulsive interaction that occurs for PG-ES1. Although this precludes high selectivity, these larger structures may be useful as sorbent materials for temperature- and pressure-swing adsorption separations. 2D-PP was found to be impermeable to all gases in these simulations, in agreement with refs 18 and 19.

■ THEORY

Langmuir Adsorption Model. Equilibrium molecular dynamics (MD) simulation results can be used to compute nonequilibrium transport across the membrane by considering the barrier crossing process in terms of free gas atoms, G_L and G_R, on the left and right side of the barrier, respectively, and the adsorbed species, A_L and A_R,

$$G_L \underset{k_d}{\overset{k_a}{\rightleftharpoons}} A_L \underset{k_0}{\overset{k_0}{\rightleftharpoons}} A_R \underset{k_a}{\overset{k_d}{\rightleftharpoons}} G_R \qquad (1)$$

An effective barrier passage rate constant, k_0, accounts for both the rate of diffusion along the surface to reach the pore and the rate of passage through the pore to the other side; we assume this is a first-order kinetic process. Assuming that the

adsorption and desorption processes are much faster than the barrier passage process, the number of adsorbed species on a particular side is in equilibrium with the free gas on that side, and can be described by the Langmuir adsorption isotherm.[31] The total concentration of adsorbed species on the left, $[A_L]$ = $[S_0]\theta_L$, where $[S_0]$ is the concentration of possible surface sites for adsorption and $\theta_L = (\alpha P_L)/(1 + \alpha P_L)$ is the fractional surface coverage, where α is a species-, surface-, and temperature-dependent adsorption equilibrium constant, and P_L is the pressure of G_L. During an equilibrium MD simulation with periodic boundary conditions (PBC), the pressure is the same on both sides, $P = P_L = P_R$, and the concentration of adsorbed species is also the same on both sides, $[A] = [A_L] = [A_L]$. The total number of bidirectional crossings observed during the simulation is the product of the reaction rate, r_{tot}, and the duration of the simulation, Δt, which is equal to the sum of the crossing rates in both directions, given by

$$r_{tot}\Delta t = 2k_0[S_0]\left(\frac{\alpha P}{1 + \alpha P}\right) \qquad (2)$$

The pressure-independent values of $k_0[S_0]$ and α can be obtained by fitting to the equilibrium MD crossing data and pressures (shown in Figure 2) obtained from several independent simulations. Crossing events were counted using the criterion of Du et al.,[26] whereby a molecule is said to have crossed the barrier if it starts as adsorbed on one side of the barrier and then crosses to the other side and remains on that other side for at least 1 ps. After the 1 ps time limit, a recrossing back to the original side is counted as another crossing event. A particle is defined as being outside the pore when it is ≥1 Å left or right of the nanoporous graphene plane, based on the probability density function shown in Figure 1. The results here are insensitive to these precise time and distance choices, and no molecules recrossed the barrier before desorbing in this simulation.
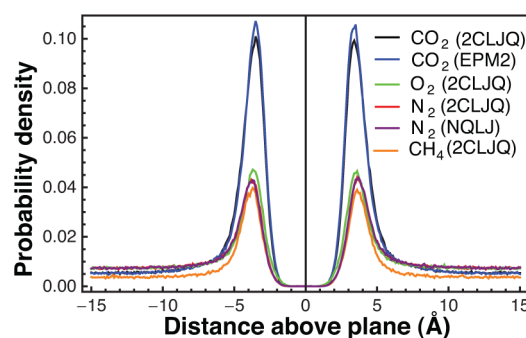

Figure 1. Probability density distribution of the molecules, as a function of distance normal to the PG-ES1 plane, from the ±60 Å simulation results.

When the pressure is different on the two sides of the membrane in eq 1, the net rate is the difference between the left→right and right→left rates,

$$r_{net} = k_0[S_0]\left(\frac{\alpha P_L}{1 + \alpha P_L} - \frac{\alpha P_R}{1 + \alpha P_R}\right) \qquad (3)$$

The permeance of a species A, p_A, is the ratio between the number of species A crossing the membrane per unit time and area, a, and the applied pressure difference across the membrane

$$p_A = \frac{r_{net,A}}{a(P_L - P_R)} \tag{4}$$

Multiplying the number of molecules that cross per Å^2 per ns per bar by 16.6054 yields the permeance in units of moles cm^{-2} bar^{-1} s^{-1}. In chemical engineering, permeance is often reported in gas permeation units (GPU), where 1 GPU = 1 × 10^{-6} (cm^3 STP) cm^{-2} (cm Hg)$^{-1}$ s^{-1}. Assuming the ideal gas equation of state for performing the conversion between moles of gas and volume of gas at standard temperature and pressure (STP), the permeance in GPU is 2.988 × 10^8 times the permeance in moles cm^{-2} bar^{-1} s^{-1}.

This direct simulation approach is conceptually simple, but is not appropriate for treating species with low vapor pressures. For example, many CO$_2$ separations also involve some amount of water vapor; at 325 K (the temperature of the simulations performed here), water is only a gas for pressures below about 0.2 atm and coexists with a liquid phase at higher pressures. Liquid droplets on the surface violate the Langmuir isotherm assumption, and liquid droplets in the gas region violate the pressure calculation assumptions. This forces us to simulate low pressures, which is inefficient because most of the computational effort is spent simulating the properties of the gas phase far from the surface. Moreover, even if the permeance of water were as high as CO$_2$, only two or three crossings would occur during a 20 ns simulation at this low pressure. (This will be further reduced because the Henry's Law constant for adsorption of water vapor on similar carbon surfaces is a third of that of CO$_2$ at these temperatures.[29]) The subsequent simulations at even lower pressures will have even fewer crossing events, making it impossible to obtain a good fit to eq 2. Studying the transport of these types of species requires more sophisticated rare-event sampling methods than used here.

The selectivity, $s_{A,B}$, describes a membrane's ability to discriminate between two species A and B. The ideal selectivity is simply the ratio of the permeances of two species. The selectivity is more rigorously defined in terms of the ratio of the mole fractions, x_A of each species in the permeate (i.e., "R", right side, products, or downstream side of the membrane) and feed (i.e., "L", left side, reactants, or upstream side of the membrane),

$$s_{A,B} = \frac{(x_{R,A}/x_{R,B})}{(x_{L,A}/x_{L,B})} \tag{5}$$

Usually, the feed mole fraction and the total pressure of the permeate are fixed quantities. Because surface adsorption can cause backcrossing, it is necessary to solve a set of simultaneous equations to obtain $x_{A,R}$. Assuming that the gases form an ideal mixture, the partial pressure of gas A is the product of its mole fraction and the total pressure (Dalton's Law), i.e.,

$$P_{L,A} = x_{L,A}P_{L,tot} \tag{6}$$

$$P_{L,B} = (1 - x_{L,A})P_{L,tot} \tag{7}$$

$$P_{R,A} = x_{R,A}P_{R,tot} \tag{8}$$

$$P_{R,B} = (1 - x_{R,A})P_{R,tot} \tag{9}$$

where we have used the fact that for a binary mixture, $x_{L,A} + x_{L,B} = 1$. According to the Langmuir adsorption isotherm, the fractional coverage of the surface in the presence of two species is given by, e.g., for species A on the left side, $\theta_{L,A} = \alpha_A P_{L,A}/(1 +$

$\alpha_A P_{L,A} + \alpha_B P_{L,B})$, where $P_{L,A}$ and $P_{L,B}$ are the partial pressures of species A and B on the left side and α_A and α_B are the adsorption constants for each of the species. This accounts for the nonideality arising from the two gases competing for surface binding sites. Similar expression can be written for both left and right sides and both A and B species. The net rate that the species cross the membrane (from eq 3) is

$$r_{net,A} = k_{0,A}[S_0](\theta_{L,A} - \theta_{R,A}) \tag{10}$$

$$r_{net,B} = k_{0,B}[S_0](\theta_{L,B} - \theta_{R,B}) \tag{11}$$

The permeate mole fraction is given by

$$x_{R,A} = \frac{r_{net,A}}{r_{net,A} + r_{net,B}} \tag{12}$$

(implicitly, $x_{R,B} = 1 - x_{R,A}$). The simultaneous solution of eqs 8–11 is sufficient to define a unique value for eq 12, and thus to determine eq 5. (Adding the constraint that $0 \leq x_{R,A} \leq 1$ speeds the numerical solution and may be necessary to obtain a unique and real value under some conditions.)

Molecular Dynamics Simulations. Equilibrium MD simulations were performed under constant particle number-volume-temperature (NVT) conditions using a Nose-Hoover thermostat set at 325 K and periodic boundary conditions using a modified version of LAMMPS 2011.11.09.[32,33] (The 2CLJQ model for N$_2$ and O$_2$ places a massless point-charge in the middle of the bond to account for the quadrupole moment. By default, LAMMPS interprets massless atoms as an error and stops the simulation, but this can be avoided by commenting out three lines in the atom.cpp files to prevent the simulation from stopping. This only works correctly if no initial velocities are assigned to the massless atoms, and the dynamics of the molecule are treated as rigid using the nvt/rigid fix in LAMMPS, as done here.) Newton's equations were integrated using 1 fs timesteps, and following a 1 ns equilibration period, position data was collected every 20 fs during a 20 ns simulation. Data collected every 2 ps was used to evaluate the probability density and compute the pressure. The PG-ES1 membrane consisted of 880 carbon and hydrogen atoms, with an area in the xy plane of 25.69 nm^2 (Figure S1B in the Supporting Information shows an example set of coordinates from the simulation). The center of mass of the PG-ES1 sheet was fixed to the geometric center of the simulation cell. Three simulations were performed for each species, having z-axis lengths of the simulation cell extending to ±45 Å, ± 60 Å, and ±120 Å for the high-, medium-, and low-pressure simulations.

Determination of the Pressure. The gas pressure is computed by determining the mean density ($1/\bar{V}$) of gas molecules in a region sufficiently far (more than 20 Å) from the PG-ES1 surface. From the ideal gas equation of state, the pressure is given by $P = RT/\bar{V}$ where $T = 325$ K is the absolute temperature and $R = 138.057$ Å^3 bar atom^{-1} K^{-1} is the gas constant in convenient units. For the temperature (325 K) and pressures (<18 bar) range considered here, the van der Waals and Redlich−Kwong equations of state for these gases[31] differ from the ideal gas results by less than the error bars on pressure in the simulation, justifying this approximation.

Force-Field Parametrization. Interactions among PG-ES1 atoms were treated using the AIREBO force-field.[34] Interactions among the gas molecules, and between gas molecules and PG-ES1 atoms were treated using a Lennard-Jones (6−12) potential, truncated and shifted at 15 Å, plus a Coulomb

interaction. The Lennard-Jones parameters for the PG-ES1 atoms were modeled using the benzene parameters of Fileti et al.,[35] as in ref.,[29] to describe the completely sp^2-hybridized hydrocarbon framework of PG-ES1. All gas molecules were treated with the 2CLJQ model of Vrabec et al.,[36] as in ref 29. Additionally, the EPM2 model for CO_2 of Harris and Yung,[37] the nonquadrupolar Lennard-Jones (NQLJ) model of N_2 of Murthy et al.,[38] (also used in ref 30), and an atomistic model of CH_4 of Stassen[39] (used to study adsorption on graphene edges in ref.[40]) were used to test the consistency of the results across various potential models. (The Stassen model results for CH_4 was only used to study the highest pressure case to verify the impermeability of PG-ES1 toward this gas.) The parameters are summarized in Table S1 in the Supporting Information. In all cases, the gas molecules are kept rigid with fixed bond lengths. Interactions between the hydrocarbon and gas parameters were described by the Lorentz−Berthelot mixing rules. For the Coulomb contribution to the force-field, the charges in the 2CLJQ, EPM2, and Stassen models were used for the gas molecules. The charges on PG-ES1 were evaluated as in ref 29. Density functional theory calculations with ABINIT 6.4.1[40] were performed on the 2 × 2 supercell shown in Figure S1A in the Supporting Information (with a 15 Å vacuum region extending normal to the plane), using the Perdew-Burke-Ernzerhof (PBE) generalized gradient exchange correlation functional, norm-conserving Trollier-Martins pseudopotentials, and a planewave energy cutoff of 50 Ry, sampling only the Γ-point of the Brillouin zone to obtain the charge density. Then, atom-centered point charges were assigned via iterative-Hirshfeld (Hirshfeld-I) analysis,[41] using promolecule all-electron atomic charge densities generated using the HF96 atomic Hartree−Fock code,[42] as described in previous work.[43] Hirshfeld-I point charges more accurately reproduce the molecular electrostatic potentials than alternative strategies such as Natural Population Analysis (NPA).[44] A small (order of 1×10^{-6}) uniform charge was added to all sites to eliminate the small (order of 1×10^{-4}) net charge on the surface arising due to rounding errors in the Hirshfeld-I calculation. A sample PG-ES1 geometry, with charges, is shown in Table S3 in the Supporting Information.

RESULTS AND DISCUSSION

Adsorption and Transport. Atomistic molecular dynamics simulations were performed at 325 K, which is the temperature of flue gas following desulfurization, the typical stage at which postcombustion carbon dioxide capture occurs. The probability density distribution (Figure 1) shows stronger adsorption of the CO_2 molecules on the surface, and weaker adsorption for the other species, in agreement with previous studies of adsorption on 2D-PP.[29] The distributions of the molecules on the surface are nearly identical for the two different force-fields, indicating that the adsorption behavior is parametrization-independent. Because the probability distribution was computed using the position of the center of each molecule, the fact that the probability density maxima occur at the same distance above the plane demonstrates that the linear molecules are adsorbed flat on the surface, rather than perpendicular to the surface. If this were not the case, then the maxima of the CO_2 molecule would be further away from the plane than that of O_2 and N_2.

Figure 2 shows the number of observed crossings across the 25.69 nm^2 membrane during a 20 ns simulation as a function of pressure. Even at the highest pressures, only two N_2 and 20 O_2
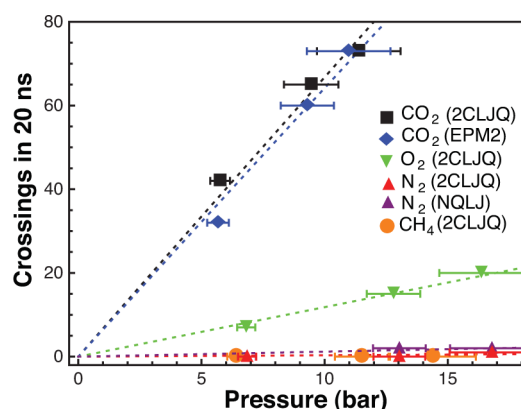

Figure 2. Barrier crossings during molecular dynamics simulation; dashed curves show the fit to eq 2, with parameters in Table S2 in the Supporting Information.

molecules cross the barrier, compared to 73 CO_2 molecules. No CH_4 molecules cross the membrane, even during an extended 50 ns simulation with either the 2CLJQ or the Stassen potential models. These results are consistent with ordering of the kinetic diameters[4] of the molecules, $CO_2 < O_2 < N_2 < CH_4$. As shown in Movie S1 in the Supporting Information, the CO_2 molecules linger on the surface before successfully crossing the barrier. Although a random incident gas molecule is unlikely to have the correct orientation to pass through the pore, the surface adsorbed species can perform multiple attempts to cross the barrier before desorption occurs.

The permeance of PG-ES1 is nearly constant with respect to pressure, under both permeate-vacuum and feed-compression conditions (Figure 3) The CO_2, O_2, and N_2 permeances are 3
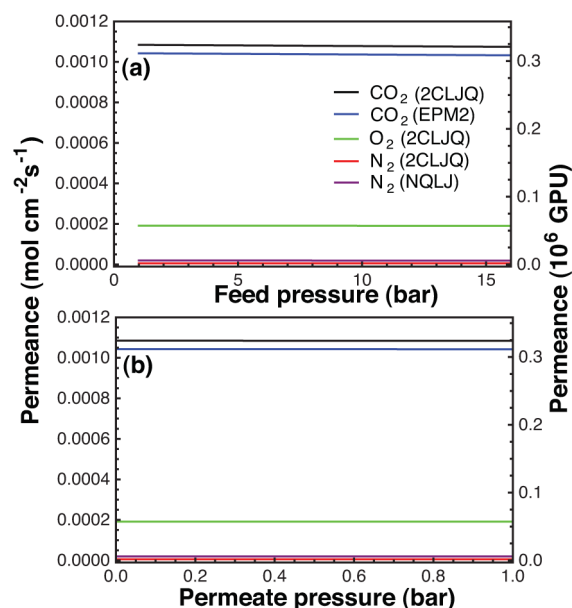

Figure 3. Single-component permeances through PG-ES1 at 325 K derived from the molecular dynamics results using the Langmuir-adsorption model, eq 4. (a) Feed compression conditions: Permeance as a function of feed pressure, with constant permeate pressure of 1 bar. (b) Permeate vacuum conditions: Permeance as a function of permeate pressure, with constant feed pressure of 1 bar. Methane is not shown, because no methane molecules were observed to transit the barrier at any pressure, even during a 50 ns simulation.

$\times$ 10^5, 6×10^4, and 6×10^3 gas permeation units (GPU), respectively, using the model with the lowest CO_2 permeance (EPM2) and the model with the highest N_2 permeance (NQLJ). (The N_2 permeance with the 2CLJQ model is lower, 2×10^3 GPU.) The CH_4 permeance is $<3 \times 10^2$ GPU, because no crossings are observed in the extended-time simulations. For comparison, MTR Polaris and 45 nm thick Polyactive films have 1×10^3 and 2×10^3 GPU CO_2 permeances, respectively.[9,45] The high CO_2 permeance of PG-ES1 may make permeate vacuum conditions (which have a lower thermodynamic cost because pressure-volume work is done on a smaller volume of gas) more economical than feed compression.[9] The fitted parameters are in Table S2 in the Supporting Information. Because αP is small for the adsorption process studied here, the system is in a linear (Henry's Law) adsorption regime. Consequently, eq 2 can be simplified to $r_{tot}\Delta t \approx 2k_0[S_0]\alpha P$ with only a single parameter, $2k_0[S_0]\alpha$, to fit the simulation data. This approximation results in a pressure-independent permeance, which is consistent with Figure 3. The more general form is preferable for two reasons: (i) In exploratory calculations conducted using noble gases, the nonlinearity and saturation of the Langmuir isotherm is necessary for describing the crossing results; (ii) This approximation removes the ability compute the competitive binding of mixtures discussed below.

The ideal selectivities are: $CO_2/N_2 = 60$, $CO_2/O_2 = 5$, $O_2/N_2 = 10$, $CO_2/CH_4 > 500$. (Again, this conservatively uses the lowest-permeance CO_2 model (EPM2) and highest permeance N_2 model (NQLJ); the lower permeance of the 2CLJQ model of N_2 increases the predicted CO_2/N_2 selectivity to 200.) For comparison, MTR Polaris and Polyactive films have CO_2/N_2 selectivities of 50 and 60, respectively.[9,45] However, high selectivity has a diminishing return, since the enrichment of the feed concentration is limited by the ratio of the permeate and feed pressures: Given feed and permeate pressures of P_f and P_p, and mole fractions of component A in the feed and permeate of $x_{A,f}$ and $x_{A,p}$, a flow of species A only occurs when $x_{A,f}P_f \geq x_{A,p}P_p$. Rearranging this yields the pressure-ratio limit, $x_{A,f}/x_{A,p} \leq P_f/P_p$, i.e., the pressure ratio sets an upper bound on the enrichment, regardless of the selectivity of the membrane. For postcombustion flue-gas membrane separations, CO_2/N_2 ideal selectivity exceeding 30 provides little benefit due to the pressure-ratio limit, since it is impractical to operate at such large pressure differences.[9] The pressure- and composition-dependent nonideal selectivities under feed compression and permeate vacuum conditions computed by solving eqs 8–12, are shown in Figure 4, using the lowest permeance EPM2 CO_2 data and the highest permeance N_2 model (NQLJ). Both conditions approach the pressure-ratio limit discussed above.

The molecular dynamics simulations above considered only pure-gas adsorption and crossing, and while the results shown in Figure 4 take into account the competitive binding to a limited number of surface sites, the gas-surface equilibrium constants used are obtained from pure-gas simulations, and this approach does not account for other types of nonideal mixture behavior that may occur. To test the validity of this approach, I performed simulations of three CO_2/N_2 mixtures (consisting of 25, 50, and 75% CO_2), under the high-pressure simulation conditions. To rule out model dependence, I considered the case where both gases were treated within the 2CLJQ model and the case with CO_2 treated using the EPM2 model and N_2 using the NQLJ model. Aside from using a gas mixture, the details of the simulation and data analysis are identical to the
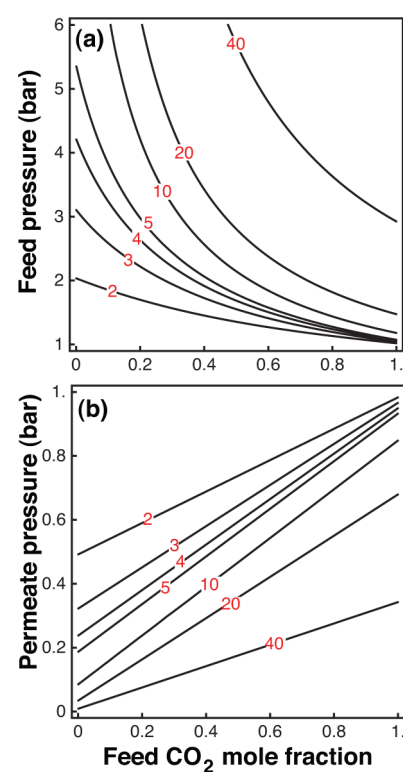

Figure 4. CO_2/N_2 selectivity of PG-ES1 at 325 K as a function of pressure and feed-composition, derived from the molecular dynamics results using the Langmuir-adsorption model. (a) Feed compression conditions: Selectivity as a function of feed pressure and CO_2 mole fraction, with constant permeate pressure of 1 bar. (b) Permeate vacuum conditions: Selectivity as a function of permeate pressure and CO_2 mole fraction, with constant feed pressure of 1 bar.

pure-gas simulations described above. The results are shown in Figure 5, as a function of the CO_2 gas-phase partial pressure.
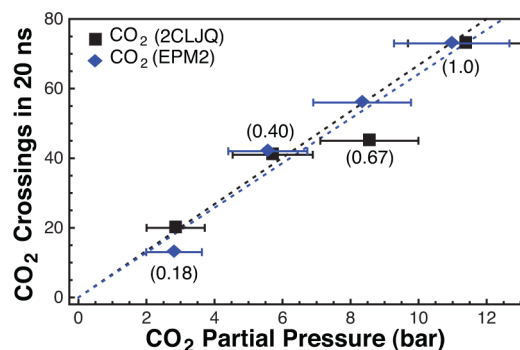

Figure 5. CO_2 barrier crossings during mixed CO_2/N_2 molecular dynamics simulation as a function of CO_2 partial pressure; dashed curves show the predicted number of crossings in the ideal (noncompetitive, noninteracting) case. Numbers in parentheses indicate the mean gas-phase CO_2 mole fractions for each pair of data points.

The mean gas-phase CO_2 mole fraction is shown in parentheses above each data point; due to the stronger surface adsorption of CO_2, a lower fraction of CO_2 is found in the gas phase than the total simulation composition. The dashed line shows the pure-CO_2 curves from Figure 2, i.e., the complete neglect of the mixture nonideality effects. There is no systematic deviation of the mixture simulation data from the ideal curve for either set

of parametrizations. This is consistent with the small adsorption equilibrium constants, α, noted above. For the temperature considered here, α for both gases is small, and for the pressures considered here, θ is far from saturation, allowing each adsorbed gas molecule to behave independently——and thus ideally.

Applications. The applications of PG-ES1 to carbon capture, methane utilization, and horticulture, are illustrated under two separation conditions: (i) feed compression with a feed pressure of 5 bar and permeate pressure of 1 bar, giving a pressure difference of $\Delta P = 4$ bar; and (ii) permeate vacuum conditions, with a feed pressure of 1 bar and a permeate pressure of 0.2 bar, giving a pressure difference of $\Delta P = 0.8$ bar. Feed compression requires more energy (since pressure-volume work is done on the entire feed supply, of which only a fraction passes through the membrane), but less membrane area (since the flux rate is linearly proportional to the pressure difference between the feed and permeate). Additionally, the capital cost of feed compression equipment tends to be lower than vacuum equipment, and there is more industrial expertise with large scale feed compression separations.[9] Permeate vacuum conditions require the least energy (since pressure-volume work is performed only on the smaller volume of the permeate), at the expense of a greater membrane area. All of the calculations use the PG-ES1 permeance of 1×10^{-3} moles CO_2 cm^{-2} bar^{-1} s^{-1} predicted by the EPM2 model.

Postcombustion Carbon Dioxide Capture. According to Matuszewski et al.,[46] the 460 coal-burning power plants in the United States emit 2×10^9 metric tons of CO_2 annually. This corresponds to 63 t CO_2 s^{-1} or 1.4×10^6 moles CO_2 s^{-1}. Under feed-compression conditions, 2×10^5 m^2 of PG-ES1 are required in total, or an average of 80 m^2 per power plant. Under permeate-vacuum conditions, 400 m^2 are required per power plant. However, to achieving 90% CO_2 capture with >95% CO_2 purity requires two separation stages,[9] which doubles the required membrane area to 160–800 m^2 per plant. According to Merkel et al.,[9] CO_2 permeances exceeding 4000 GPU and with CO_2/N_2 selectivity >40 allow for membrane-based postcombustion capture at below $15/ton CO_2. PG-ES1 far surpasses these demands, and thus is the first material capable of meeting the U.S. Department of Energy's goal of $20/ton CO_2. Because the cost estimate provided by Merkel et al. is based on the scaled capital cost of the membrane per GPU, PG-ES1 meets this cost target so long as it is less than 100 times as expensive (per area) as the benchmark MTR-Polaris membrane used in that study.

Methane Upgrading. The high CO_2/CH_4 selectivity would also be useful for upgrading biogenic ("landfill") methane,[8] which typically consists of equal concentrations of these two species. According to Patel et al.,[47] the Brookhaven, New York, municipal landfill produces 17.4×10^6 m^3 CH_4 per year mixed with an equal quantity of CO_2. This corresponds to 24.6 mols CO_2 s^{-1} to be removed (assuming the gas is at STP). This requires 0.6 m^2 or 3 m^2 PG-ES1 under feed-compression and permeate-vacuum conditions, respectively.

Horticulture. Membrane-based purification of atmospheric CO_2 is infeasible due to the pressure-ratio limit, since the small concentration (roughly 350 ppm) requires an impractical number of stages with feasible feed and permeate pressures. However, some applications benefit from enriching, rather than purifying, this dilute CO_2. For example, plant growth in greenhouses can be accelerated by increasing the concentration

of CO_2 from the atmospheric level to approximately 1000 ppm, which is only a factor of 3 in concentration, and could be performed in a single stage. A small (20 m^3) greenhouse contains about 900 mols of gas at STP, of which 0.3 mols are CO_2; to triple this we must add 0.6 mol CO_2/hour (assuming a complete air exchange once per hour). This requires 0.04 cm^2 or 0.2 cm^2 PG-ES1 under feed-compression and vacuum-permeate conditions, respectively. If the vacuum-permeate separation is performed as an isothermal, reversible process, less than 1 W-hour of work is required each hour ($(0.6$ mol $CO_2)$ $RT\ln(0.2)$), where $RT = 2.479$ kJ/mol at 25 °C. This lower-bound ignores the inefficiency of the vacuum pump and work done on oxygen and nitrogen, but even with one- or two-orders of magnitude energy inefficiency could be powered by a small photovoltaic system. Since CO_2 enrichment is only needed during daylight hours when the plants perform photosynthesis, no battery storage is needed for this application.

Feasibility. It should be possible to synthesize PG-ES1 following a similar strategy as the porous graphene synthesis of Bieri et al.[16] First, a ring-shaped monomer, appropriately substituted with halogen atoms, would be synthesized using organic chemistry techniques. Second, the ring-shaped monomer (which is likely a solid at standard temperature and pressure due to its molecular weight) can be heating in a crucible in a vacuum to vaporize the material and deposit the vapor on a metal surface. Third, heating the metal surface catalyzes dehalogenation of the ring-shaped monomeric precursors, desorption of the halogen atoms, and aryl−aryl coupling of the dehalogenated monomers to yield the two-dimensional polymer.[16] (A similar strategy has also been used to create one-dimensional hydrocarbon polymers.[50]) Many combinations of halogens and metal surfaces undergo this type of reaction.[51,52] Although existing nanoporous graphene membranes have not yet been synthesized at the large areas needed for some of these applications,[16,20] ongoing research in the production of high-quality, large-area graphene films[48,49] could be adapted to produce nanoporous materials such as PG-ES1.

While a large-area contiguous sheet of PG-ES1 would be ideal, it is also possible to incorporate small flakes into existing membrane materials to increase their permeance. For example, May et al. recently demonstrated the direct incorporation of micrometer-sized graphene flakes into polyvinyl alcohol without having to go through a graphene oxide intermediate,[53] which is particularly relevant because it avoids potentially detrimental oxidative damage to the PG-ES1 structure. May et al. found in-plane alignment of the graphene flakes within the polymer sheet, which maximizes the exposed area of the PG-ES1 flakes in the direction of gas transport and also maximizes the mechanical strength of the resulting composite. Incorporating PG-ES1 into an existing high-performance carbon dioxide separation membrane (such as MTR Polaris™ or Polyactive™ discussed above) would enable a reduction of the thickness of the resulting composite while maintaining sufficient mechanical strength. Since membrane permeance is inversely proportional to thickness, the resulting thinner composite material will have a higher permeance than the starting material. The very high permeance of PG-ES1 will not impede carbon dioxide transport, while maintaining a favorably high selectivity against transport of other gases.

CONCLUSION

From a fundamental perspective, this study introduces a Langmuir-adsorption model for calculating the effect of surface adsorption of gases on membrane permeance from MD simulations. This model can be used to predict gas transport through the growing variety of two-dimensional porous materials.[16,20,54] Tuning the surface adsorption, e.g., by fluorinating the surface reduces the attractive dispersion interactions (hence reducing surface adsorption) or by using a nonuniform charge distribution to increase the adsorption of dipolar molecules,[29] provides an additional means of controlling the transport of molecules through nanoporous materials. A similar effect based on differential wetting of the surface may also be relevant to liquid mixture separations, with the adsorption tuned by surface modifications (e.g., hydrophobic or hydrophilic surface modifications) and the charge distribution within the nanoporous sheet (e.g., interaction with ions or polar molecules).

From a technological perspective, PG-ES1 is capable of unprecedented permeance and selectivity for CO_2 separation from N_2 and CH_4. PG-ES1 is the first material capable of meeting the cost targets for postcombustion carbon dioxide capture, which has profound implications for widespread economic implementation of postcombustion carbon dioxide capture on fossil fuel plants, as well as other applications.

ASSOCIATED CONTENT

Ⓢ Supporting Information

Force-field parameters, fitted isotherm parameters, sample PG-ES1 geometry with charges, and a movie of the CO_2 crossing process from the molecular dynamics simulation. This material is available free of charge via the Internet at http://pubs.acs.org/.

AUTHOR INFORMATION

Corresponding Author

*E-mail: jschrier@haverford.edu.

Notes

The authors declare the following competing financial interest(s): I have submitted a US Provisional Patent Application for the PG-ES1 material described in this paper.

ACKNOWLEDGMENTS

REFERENCES

(1) Climate Change 2007: Synthesis Report. Contribution of Working Groups I, II and III to the Fourth Assessment Report of the Intergovernmental Panel on Climate Change; Pauchauri, R. K., Reisinger, A., Eds.; IPCC: Geneva, Switzerland, 2007.

(2) D'Alessandro, D. M.; Smit, B.; Long, J. R. Angew. Chem., Int. Ed. 2010, 49, 6058−6082.

(3) Bernardo, P.; Drioli, E.; Golemme, G. Ind. Eng. Chem. Res. 2009, 48, 4638−4663.

(4) Scholes, C. A.; Kentish, S. E.; Stevens, G. W. Rec. Pat. Chem. Eng. 2008, 1, 52−66.

(5) Du, N.; Park, H. B.; Dal-Cin, M. M.; Guiver, M. D. Energy Environ. Sci. 2012, 5, 7406−7322.

(6) Ismail, A. F.; Rana, D.; Matsuura, T.; Foley, H. C. Carbon-Based Membranes for Separations; Springer: New York, 2011.

(7) Sumida, K.; Rogow, D. L.; Mason, J. A.; McDonald, T. M.; Bloch, E. D.; Herm, Z. R.; Bae, T.-H.; Long, J. R. Chem. Rev. 2012, 112, 724−781.

(8) Baker, R. W.; Lokhandwala, K. Ind. Eng. Chem. Res. 2008, 47, 2109−2121.

(9) Merkel, T. C.; Lin, H.; Wei, X.; Baker, R. J. Membr. Sci. 2010, 359, 126−139.

(10) Favre, E. Chem. Eng. J. 2011, 171, 782−793.

(11) Bunch, J. S.; Verbridge, S. S.; Alden, J. S.; van der Zande, A. M.; Parpia, J. M.; Craighead, H. G.; McEuen, P. L. Nano Lett. 2008, 8, 2458−2462.

(12) Leenaerts, O.; Partoens, B.; Peeters, F. M. Appl. Phys. Lett. 2008, 93, 193107.

(13) Sing, K.; Wang, B.; Král, P. J. Am. Chem. Soc. 2008, 130, 16448−16449.

(14) Suk, M. E.; Aluru, N. R J. Phys. Chem. Lett. 2010, 1, 1590−1594.

(15) Jiang, D.; Cooper, V. R.; Dai, S. Nano Lett. 2009, 9, 4019−4024.

(16) Bieri, M.; Trier, M.; Cai, J.; Aït-Mansour, K.; Ruffieux, P.; Gröning, O.; Gröning, P.; Kastler, M.; Rieger, R.; Feng, X.; Müllen, K.; Fasel, R. Chem. Commun. 2009, 6919−6921.

(17) Li, Y.; Zhou, Z.; Shen, P.; Chen, Z. Chem. Commun. 2010, 46, 3672−3674.

(18) Blankenburg, S.; Bieri, M.; Fasel, R.; Müllen, K.; Pignedoli, C. A.; Passerone, D. Small 2010, 6, 2266−2271.

(19) Schrier, J. J. Phys. Chem. Lett. 2010, 1, 2284−2287.

(20) Li, G.; Li, Y.; Liu, H.; Guo, Y.; Li, Y.; Zhu, D. Chem. Commun. 2010, 46, 3256−3258.

(21) Jiao, Y.; Du, A.; Hankel, M.; Zhu, Z.; Rudolph, V.; Smith, S. C. Chem. Commun. 2011, 47, 11843−11845.

(22) Schrier, J.; McClain, J. Chem. Phys. Lett. 2012, 521, 118−124.

(23) Hauser, A. W.; Schwerdtfeger, P. J. Phys. Chem. Lett. 2012, 3, 209−213.

(24) Hankel, M.; Jiao, Y.; Du, A.; Gray, S. K.; Smith, S. C. J. Phys. Chem. C 2012, 116, 6672−6676.

(25) Hauser, A. W.; Schrier, J.; Schwerdtfeger, P. J. Phys. Chem. C 2012, 116, 10819−10827.

(26) Du, H.; Li, J.; Zhang, J.; Su, G.; Li, X.; Zhao, Y. J. Phys. Chem. C 2011, 115, 23261−23266.

(27) Krapivsky, P. L.; Redner, S.; Ben-Naim, E. A Kinetic View of Statistical Physics; Cambridge University Press: Cambridge, U.K., 2010.

(28) Berezhkovskii, A. M.; Barzykin, A. V. J. Chem. Phys. 2012, 136, 054115.

(29) Schrier, J. ACS Appl. Mater. Interfaces 2011, 3, 4451−4458.

(30) Babarao, R.; Dai, S.; Jiang, D. J. Phys. Chem. C 2012, 116, 7106−7110.

(31) McQuarrie, D. A.; Simon, J. D. Physical Chemistry: A Molecular Approach; University Science Books: Sausalito, CA, 1997.

(32) Plimpton, S. J. Comput. Phys. 1995, 117, 1−19.

(33) http://lammps.sandia.gov.

(34) Stuart, S. J.; Tutein, A. B.; Harrison, J. A. J. Chem. Phys. 2000, 112, 6472−6486.

(35) Fileti, E. E.; Dalpian, G. M.; Rivelino, R. J. Appl. Phys. 2010, 108, 113527.

(36) Vrabec, J.; Stoll, J.; Hasse, H. J. Phys. Chem. B 2001, 105, 12126−12133.

(37) Harris, J. G.; Yung, K. H. J. Phys. Chem. 1995, 99, 12021−12024.

(38) Murthy, C. S.; Singer, K.; Klein, M. L.; McDonald, I. R. Mol. Phys. 1980, 41, 1387−1399.

(39) Stassen, H. J. Mol. Struct.: THEOCHEM 1999, 464, 107−119.

(40) Gonze, X.; Amadon, B.; Anglade, P.-M.; Beuken, J.-M.; Bottin, F.; Boulanger, P.; Bruneval, F.; Caliste, D.; Caracas, R.; Côté, M.; et al. *Comput. Phys. Commun.* **2009**, *180*, 2582−2615.

(41) Bultinck, P.; Van Alsenoy, C.; Ayers, P. W.; Carbó-Dorca, R. *J. Chem. Phys.* **2007**, *126*, 144111.

(42) Froese Fischer, C.; Gaigalas, G. *Comput. Phys. Commun.* **1996**, *98*, 255−264.

(43) Glor, E. C.; Blau, S. M.; Yeon, J.; Zeller, M.; Halasyamani, P. S.; Schrier, J.; Norquist, A. J. *J. Solid State Chem.* **2011**, *184*, 1445−1450.

(44) Van Damme, S.; Bultinck, P.; Fias, S. *J. Chem. Theory Comput.* **2009**, *5*, 334−340.

(45) Yave, W.; Car, A.; Wind, J.; Peinemann, K.-V. *Nanotechnology* **2010**, *21*, 395301.

(46) Matuszewski, M.; Ciferno, J.; Marano, J. J.; Chen, S. *Research and Development Goals for CO$_2$ Capture Technology*; DOE/NETL-2009/1366; National Energy Technology Laboratory: Pittsburgh, PA; 2011.

(47) Patel, S.; Tonjes, D.; Mahajan, D. *J. Renewable Sustainable Energy* **2011**, *3*, 043118.

(48) Bae, S.; Lee, Y.; Xu, X.; Park, J.-S.; Zheng, Y.; Balakrishnan, J.; Lei, T.; Kim, H. R.; Song, Y. I.; et al. *Nat. Nanotechnol.* **2010**, *5*, 574−578.

(49) Jo, S. B.; Park, J.; Lee, W. H.; Cho, K.; Hong, B. H. *Solid State Commun.* **2012**, in press, doi:10.1016/j.ssc.2012.04.056.

(50) Cai, J.; Ruffieux, P.; Jaafar, R.; Bieri, M.; Braun, T.; Blankenburg, S.; Muoth, M.; Seitsonen, A. P.; Saleh, M.; Feng, X.; Müllen, K.; Fasel, R. *Nature* **2010**, *466*, 470−473.

(51) Gutzler, R.; Walch, H.; Eder, G.; Kloft, S.; Heckl, W. M.; Lackinger, M. *Chem. Commun.* **2009**, 4456−4458.

(52) Walch, H.; Gutzler, R.; Sirtl, T.; Eder, G.; Lackinger, M. *J. Phys. Chem. C* **2010**, *114*, 12604−12609.

(53) May, P.; Khan, U.; O'Neill, A.; Coleman, J. N. *J. Mater. Chem.* **2012**, *22*, 1278−1282.

(54) Brunetto, G.; Autreto, P. A. S.; Machado, L. D.; Santos, B. I.; dos Santos, R. P. B.; Galvão, D. S. *J. Phys. Chem. C* **2012**, *116*, 12810−12813.